Biomedical Optics EXPRESS

Toward fast malaria detection by secondary speckle sensing microscopy

Dan Cojoc,[1,*] Sara Finaurini,[1] Pavel Livshits,[2] Eran Gur,[3] Alon Shapira,[4] Vicente Mico,[5] and Zeev Zalevsky[2,6]

[1]*Istituto Officina dei Materiali IOM-CNR, Area Science Park—Basovizza, S.S. 14 km 163.5, Trieste 34149, Italy*
[2]*Faculty of Engineering, Bar-Ilan University, Ramat-Gan 52900, Israel*
[3]*Jerusalem College of Engineering, Dept. of Electronics, Jerusalem 91035, Israel*
[4]*Dept. of Mathematics, Bar-Ilan University, Ramat-Gan 52900, Israel*
[5]*Departamento de Óptica, Universitat de València, c/Dr. Moliner, 50, 46100 Burjassot, Spain*
[6]*Erlangen Graduate School in Advanced Optical Technologies (SAOT), Friedrich-Alexander Universität Erlangen-Nürnberg, Paul-Gordan-Straße 6, 91052 Erlangen, Germany*
**cojoc@iom.cnr.it*

Abstract: Diagnosis of malaria must be rapid, accurate, simple to use, portable and low cost, as suggested by the World Health Organization (WHO). Despite recent efforts, the gold standard remains the light microscopy of a stained blood film. This method can detect low parasitemia and identify different species of *Plasmodium*. However, it is time consuming, it requires well trained microscopist and good instrumentation to minimize misinterpretation, thus the costs are considerable. Moreover, the equipment cannot be easily transported and installed. In this paper we propose a new technique named "secondary speckle sensing microscopy" (S^3M) based upon extraction of correlation based statistics of speckle patterns generated while illuminating red blood cells with a laser and inspecting them under a microscope. Then, using fuzzy logic ruling and principle component analysis, good quality of separation between healthy and infected red blood cells was demonstrated in preliminary experiments. The proposed technique can be used for automated high rate detection of malaria infected red blood cells.

OCIS codes: (170.4580) Optical diagnostics for medicine; (170.3880) Medical and biological imaging; (170.1530) Cell analysis; (170.0180) Microscopy; (120.6160) Speckle interferometry; (170.1470) Blood or tissue constituent monitoring; (170.6480) Spectroscopy, speckle.

References and links

1. WHO, ed., "World Malaria Report: 2010," in WHO Library Cataloguing in Publication Data, *http://www.who.int/malaria/world_malaria_report_2010/en/index.html*.
2. WHO, "Microscopy Quality Assurance Manual" (2009), *http://www.searo.who.int/LinkFiles/Malaria_MalariaMicroscopyManual*.
3. C. K. Murray, R. A. Gasser, Jr., A. J. Magill, and R. S. Miller, "Update on rapid diagnostic testing for malaria," Clin. Microbiol. Rev. **21**(1), 97–110 (2008).
4. C. Wongsrichanalai, M. J. Barcus, S. Muth, A. Sutamihardja, and W. H. Wernsdorfer, "A review of malaria diagnostic tools: microscopy and rapid diagnostic test (RDT)," Am. J. Trop. Med. Hyg. **77**(6 Suppl), 119–127 (2007).
5. Centers for Disease Control and Prevention, "Malaria," *www.cdc.gov/malaria*.
6. A. Fontaine, S. Bourdon, M. Belghazi, M. Pophillat, P. Fourquet, S. Granjeaud, M. Torrentino-Madamet, C. Rogier, T. Fusai, and L. Almeras, "*Plasmodium falciparum* infection-induced changes in erythrocyte membrane proteins," Parasitol. Res. **110**(2), 545–556 (2012).
7. A. G. Maier, B. M. Cooke, A. F. Cowman, and L. Tilley, "Malaria parasite proteins that remodel the host erythrocyte," Nat. Rev. Microbiol. **7**(5), 341–354 (2009).
8. J. P. Shelby, J. White, K. Ganesan, P. K. Rathod, and D. T. Chiu, "A microfluidic model for single-cell capillary obstruction by *Plasmodium falciparum*-infected erythrocytes," Proc. Natl. Acad. Sci. U.S.A. **100**(25), 14618–14622 (2003).
9. J. P. Mills, M. Diez-Silva, D. J. Quinn, M. Dao, M. J. Lang, K. S. W. Tan, C. T. Lim, G. Milon, P. H. David, O. Mercereau-Puijalon, S. Bonnefoy, and S. Suresh, "Effect of plasmodial RESA protein on deformability of human red blood cells harboring *Plasmodium falciparum*," Proc. Natl. Acad. Sci. U.S.A. **104**(22), 9213–9217 (2007).

#162404 - $15.00 USD Received 3 Feb 2012; revised 15 Mar 2012; accepted 23 Mar 2012; published 18 Apr 2012

10. A. M. Dondorp, K. T. Chotivanich, S. Fucharoen, K. Silamut, J. Vreeken, P. A. Kager, and N. J. White, "Red cell deformability, splenic function and anaemia in thalassaemia," Br. J. Haematol. **105**(2), 505–508 (1999).
11. A. M. Dondorp, P. A. Kager, J. Vreeken, and N. J. White, "Abnormal blood flow and red blood cell deformability in severe malaria," Parasitol. Today (Regul. Ed.) **16**(6), 228–232 (2000).
12. F. Omodeo-Salè, A. Motti, N. Basilico, S. Parapini, P. Olliaro, and D. Taramelli, "Accelerated senescence of human erythrocytes cultured with *Plasmodium falciparum*," Blood **102**(2), 705–711 (2003).
13. F. Omodeo-Salè, A. Motti, A. Dondorp, N. J. White, and D. Taramelli, "Destabilisation and subsequent lysis of human erythrocytes induced by *Plasmodium falciparum* haem products," Eur. J. Haematol. **74**(4), 324–332 (2005).
14. C. A. Moxon, G. E. Grau, and A. G. Craig, "Malaria: modification of the red blood cell and consequences in the human host," Br. J. Haematol. **154**(6), 670–679 (2011).
15. M. G. Millholland, R. Chandramohanadas, A. Pizzarro, A. Wehr, H. Shi, C. Darling, C. T. Lim, and D. C. Greenbaum, "The malaria parasite progressively dismantles the host erythrocyte cytoskeleton for efficient egress," Mol. Cell. Proteomics **10**(12), M111.010678 (2011).
16. S. Suresh, J. Spatz, J. P. Mills, A. Micoulet, M. Dao, C. T. Lim, M. Beil, and T. Seufferlein, "Connections between single-cell biomechanics and human disease states: gastrointestinal cancer and malaria," Acta Biomater. **1**(1), 15–30 (2005).
17. L. Gervais, N. de Rooij, and E. Delamarche, "Microfluidic chips for point-of-care immunodiagnostics," Adv. Mater. (Deerfield Beach Fla.) **23**(24), H151–H176 (2011).
18. R. Fan, O. Vermesh, A. Srivastava, B. K. H. Yen, L. Qin, H. Ahmad, G. A. Kwong, C.-C. Liu, J. Gould, L. Hood, and J. R. Heath, "Integrated barcode chips for rapid, multiplexed analysis of proteins in microliter quantities of blood," Nat. Biotechnol. **26**(12), 1373–1378 (2008).
19. R. Lima, T. Ishikawa, Y. Imai, M. Takeda, S. Wada, and T. Yamaguchi, "Radial dispersion of red blood cells in blood flowing through glass capillaries: the role of hematocrit and geometry," J. Biomech. **41**(10), 2188–2196 (2008).
20. H. W. Hou, A. A. S. Bhagat, A. G. L. Chong, P. Mao, K. S. W. Tan, J. Han, and C. T. Lim, "Deformability based cell margination--a simple microfluidic design for malaria-infected erythrocyte separation," Lab Chip **10**(19), 2605–2613 (2010).
21. H. Bow, I. V. Pivkin, M. Diez-Silva, S. J. Goldfless, M. Dao, J. C. Niles, S. Suresh, and J. Han, "A microfabricated deformability-based flow cytometer with application to malaria," Lab Chip **11**(6), 1065–1073 (2011).
22. G. Popescu, T. Ikeda, R. R. Dasari, and M. S. Feld, "Diffraction phase microscopy for quantifying cell structure and dynamics," Opt. Lett. **31**(6), 775–777 (2006).
23. G. Popescu, Y. Park, W. Choi, R. R. Dasari, M. S. Feld, and K. Badizadegan, "Imaging red blood cell dynamics by quantitative phase microscopy," Blood Cells Mol. Dis. **41**(1), 10–16 (2008).
24. G. Popescu, Y. K. Park, K. Badizadegan, R. R. Dasari, and M. S. Feld, "Diffraction phase and fluorescence microscopy," Opt. Express **14**(18), 8263–8268 (2006).
25. Y. Park, M. Diez-Silva, G. Popescu, G. Lykotrafitis, W. Choi, M. S. Feld, and S. Suresh, "Refractive index maps and membrane dynamics of human red blood cells parasitized by *Plasmodium falciparum*," Proc. Natl. Acad. Sci. U.S.A. **105**(37), 13730–13735 (2008).
26. N. Lue, W. Choi, G. Popescu, Z. Yaqoob, K. Badizadegan, R. R. Dasari, and M. S. Feld, "Live cell refractometry using Hilbert phase microscopy and confocal reflectance microscopy," J. Phys. Chem. A **113**(47), 13327–13330 (2009).
27. C. S. Yelleswarapu, M. Tipping, S. R. Kothapalli, A. Veraksa, and D. V. Rao, "Common-path multimodal optical microscopy," Opt. Lett. **34**(8), 1243–1245 (2009).
28. N. Pavillon, A. Benke, D. Boss, C. Moratal, J. Kühn, P. Jourdain, C. Depeursinge, P. J. Magistretti, and P. Marquet, "Cell morphology and intracellular ionic homeostasis explored with a multimodal approach combining epifluorescence and digital holographic microscopy," J Biophotonics **3**(7), 432–436 (2010).
29. Y. Park, M. Diez-Silva, D. Fu, G. Popescu, W. Choi, I. Barman, S. Suresh, and M. S. Feld, "Static and dynamic light scattering of healthy and malaria-parasite invaded red blood cells," J. Biomed. Opt. **15**(2), 020506 (2010).
30. Z. Zalevsky and J. Garcia, "Motion detection system and method," Israeli Patent Application No. 184868 (July 2007); WO/2009/013738 International Application No. PCT/IL2008/001008 (July 2008).
31. Y. Beiderman, A. D. Amsel, Y. Tzadka, D. Fixler, V. Mico, J. Garcia, M. Teicher, and Z. Zalevsky, "A microscope configuration for nanometer 3-D movement monitoring accuracy," Micron **42**(4), 366–375 (2011).
32. Y. Beiderman, I. Horovitz, N. Burshtein, M. Teicher, J. Garcia, V. Mico, and Z. Zalevsky, "Remote estimation of blood pulse pressure via temporal tracking of reflected secondary speckles pattern," J. Biomed. Opt. **15**(6), 061707 (2010).
33. Y. Beiderman, R. Blumenberg, N. Rabani, M. Teicher, J. Garcia, V. Mico, and Z. Zalevsky, "Demonstration of remote optical measurement configuration that correlates to glucose concentration in blood," Biomed. Opt. Express **2**(4), 858–870 (2011).
34. W. Trager and J. B. Jensen, "Human malaria parasites in continuous culture," Science **193**(4254), 673–675 (1976).
35. L. A. Zadeh, "Fuzzy sets," Inf. Control **8**(3), 338–353 (1965).
36. M. Schneider, A. Kandel, G. Langholz, and G. Chew, *Fuzzy Expert System Tools* (Wiley, 1996).
37. E. Gur, D. Mendlovic, and Z. Zalevsky, "Optical implementation of fuzzy-logic controllers. Part I," Appl. Opt. **37**(29), 6937–6945 (1998).
38. K. Pearson, "On lines and planes of closest fit to systems of points in space," Philos. Mag. **2**, 559–572 (1901).

#162404 - $15.00 USD Received 3 Feb 2012; revised 15 Mar 2012; accepted 23 Mar 2012; published 18 Apr 2012

39. S. Wold, K. Esbensen, and P. Geladi, "Principal component analysis," Chemom. Intell. Lab. Syst. **2**(1-3), 37–52 (1987).

1. Introduction

Malaria is an infectious disease caused by the bite of a female anopheles mosquito infected by *Plasmodium*. Every year, 243 million new cases are reported by the World Health Organization (WHO) with almost a million deaths, mostly of African children. Due to the nonspecific symptoms (fever) and the absence of a rapid and efficient diagnostic tool, presumptive antimalarial treatment is often preferred. This increases the risk of mortality due to inappropriate therapy and favors the emergence of drug resistance. Thus, new tools for a prompt and accurate malaria diagnosis are urgently needed [1].

The ideal diagnostic tool for malaria in endemic countries must be rapid, accurate, simple to use, low cost, and easily interpretable. The gold standard in malaria diagnosis is the microscopic Giemsa-stained blood smear (MSB), which remains the only method allowing detection with high sensitivity and specificity. Low parasitemia (0.0001%, i.e., 1 infected cell over 10^6 cells) detection and identification of the parasite species (*Plasmodium falciparum*, *Plasmodium vivax*, *Plasmodium malariae*, *Plasmodium ovale*) are thus possible [2,3].

However, misinterpretation (artifacts mistaken for malaria parasite such as fungi, bacteria, or cell debris) can commonly occur in poor setting laboratories with low quality microscopes where only the experience of a well-trained microscopist can reduce the errors [2,4]. The time to diagnosis is about 8-10 hours in African medical centers [2]. The cost of equipment and training is considerable, even if the apparent cost for an individual sample examination is relatively low. Moreover, the equipment cannot be easily transported and installed. An improvement of diagnostic tools is in this context highly demanded. New innovative technologies could be used to enhance the accuracy while reducing time, complexity and cost of actual diagnosis.

Malaria symptoms (fever, swear etc.) are associated with the asexual intraerythrocytic life cycle of the parasite. After the initial replication inside the hepatocytes, the merozoites invade the host red blood cells (RBC), where they grow adopting different morphologies from the early ring shape to the late trophozoite. At this stage, the parasites undergo several cellular division forming schizonts which release 16-32 new merozoites into the blood stream after erythrocytic membrane disruption [5].

The parasite development continuously remodels the membrane and cytoskeleton of the host RBC. Modification of more than 100 proteins of the host RBC proteome that could have an important impact on the morphology and rheological properties of the infected RBC (iRBC) and on malaria pathogenesis have been recently reported [6]. Most of them are exported to the iRBC surface. These make iRBC membrane more adhesive promoting thereby the cytoadherence [7]. Progressive stiffness of the cell membrane is also associated with the parasite grow [8]. Stiffness influences deformabiltiy. Thus, deformability is mildly reduced in rings (increased sphericity) and markedly altered in schizonts [9]. Seminal studies in *P. falciparum*-infected patients have established a correlation between a decreased elongation index of the circulating RBC population and anemia or poor prognosis [10]. The biomechanical properties of the uninfected RBCs (uRBC) present in parasitized blood are also altered in vitro and in vivo, but the mechanism and the causes are still unclear [11–14]. Molecular biology and proteomics are largely used to investigate the membrane structures in both healthy and parasitized RBC [15]. However, these techniques cannot fully explain the biomechanical modifications (such as elasticity, deformability and stiffness) occurring during malaria infection.

There are several techniques available nowadays to measure biomechanical changes of the cells. They can be classified in: microfluidics and optical techniques. Microfluidics is based on recent progresses in micro and nanofabrication techniques and use of new materials which make possible to create microchannels and flows with properties similar to that of the blood vessels [16,17]. Exploiting the hemodynamic effects (e.g. Fahraeus effect, margination) of the cells in a microfluidic flow, plasma separation [18] and white blood cell (WBC) enrichment

#162404 - $15.00 USD Received 3 Feb 2012; revised 15 Mar 2012; accepted 23 Mar 2012; published 18 Apr 2012

[19] have been proposed. The margination effect, based on the deformability of RBCs, has recently been used for separation of malaria iRBCs [20]. The performance, in terms of accuracy, is still far from that of MSB, but can be used as an iRBCs pre-concentration approach. A microfabricated deformability-based flow cytometer with micro-pillars having suitable size, shape and gap between them, has also been proposed for the separation of iRBCs [21]. However, since the gap between the pillars is used to filter the cells by their size, the channels are rapidly obstructed during the separation process, thereby limiting the use of the device.

Alternatively, optical techniques are mainly based on novel diffraction microscopy schemes, made possible by the development of new laser sources and fast and sensitive detectors. Diffraction phase microscopy (DPM) [22] has been proposed for a more accurate characterization of the dynamics of the cell membrane, and hence its stiffness, and the composition of the cell [23]. Moreover, multimodal imaging in microscopy provided by the combination of different techniques is a valuable tool for quantifying information about cell dynamics and evolutions at nanoscale range by cross-checking information between them [24–29]. Measuring the stiffness from the thermal fluctuations of the membrane, Park *et al.* present the comparative results for healthy and infected RBC at different erythrocytic stages [25]. The mean determined shear modulus varies from 14 μN/m for ring, to 72 μN/m for schizont, while for healthy RBC it is only 6 μN/m.

Nevertheless, the distributions for each RBC type are characterized by large standard deviations and hence there is a considerable overlap between the data making difficult a clear separation. Considering that the membrane fluctuations at different points of the cells are measured accurately, it is likely that the results of this measurement be processed to extract more features than the stiffness only. The same method allows to obtain the refractive index map of the cell and hence information about the structure of RBC. However, the implementation of this technique is still at the lab level, requiring a relatively expensive instrumentation which cannot be easily transported. Moreover, only a reduced number of cells can be processed per unit of time.

In this paper we propose an adjustment of the secondary speckle sensing approach described in Refs. [30–33] for the implementation of rapid, high rate and high accuracy automatic detection of malaria. The approach involves illuminating the RBCs with a tilted laser beam. The microscope, by properly adjusting its focus, captures time varied speckle patterns generated due to the thermal movement of the RBCs. This movement is analyzed via correlation based algorithm that extracts the change in the position and in the value of the correlation peak. Then, the statistics related to the position and value of the correlation peak is analyzed using two automated approaches: fuzzy logic based ruling and principle component analysis (PCA). In this paper we construct the full system as well as the automatic detection algorithmic and present in preliminary experimental results the potential for automatic detection of malaria.

Note that basically, the main difference between the speckle based technique and quantitative methods in phase microscopy is the simplicity of realization or the simplicity in the calibration stage of the optical setup. The speckle based approach is also directly related to physical value. It measures directly the movements of the cells and not the phase that is changed due to those movements. It is also simpler to translate the movement of the cell (i.e. the size of movement and the direction of movement) to the change we obtain in the speckle pattern. It is also relatively simpler, using the proposed speckle based approach, to tune the sensitivity of detection, i.e. how small is the movement of the cell that still may be detected by this technique e.g. in the Z (axial) direction. This is done simply by changing the defocusing of the objective lens. Defocusing also changes the size of the speckle patterns which also affects the measurement sensitivity.

The paper is constructed as follows: in Section 2 we present the optical setup, and in Section 3 the experimental results. Section 4 addresses the fuzzy logic based algorithm, while Section 5 focuses on the PCA algorithm. Section 6 concludes the paper.

#162404 - $15.00 USD Received 3 Feb 2012; revised 15 Mar 2012; accepted 23 Mar 2012; published 18 Apr 2012

2. Secondary speckle sensing microscopy (S^3M) setup

The S^3M setup is depicted in Fig. 1 and consists of a custom inverted microscope in which the sample is illuminated by a tilted laser beam (Ar^+ 514.5 nm, LaserPhysics, Cheshire, UK). Additionally, an on-axis white light fiber optic illuminator is used for reference imaging and alignment purposes only. Note that the tilted laser was used due to mechanical/physical constraints of the constructed system as well as in order to avoid direct reflections of the laser into the camera. The defocusing is needed in order to convert the titling movement into shifts since linear phase addition becomes a shift in the Fourier domain (far field approximation) and shifts can easily be detected by correlation based computations as those being applied in this paper.

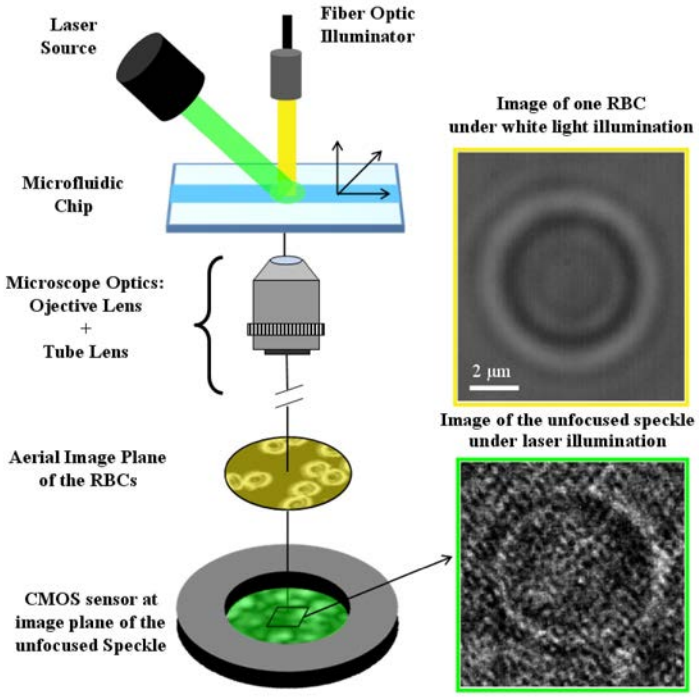

Fig. 1. Secondary speckle sensing microscopy (S^3M) optical setup.

The sample is imaged by an objective (PL APO 100x/1 water, Olympus) and a tube lens (achromatic doublet, f = 300 mm) onto the sensor of a CMOS camera (Fastec Hispec-4, from Gold Elettronica, Chiavari, Italy). After cell identification, the sample is moved several micrometers upside on the optical axis allowing that an unfocused image of the speckle pattern be recorded on the CMOS camera. As an example, Fig. 1 (right) shows the image of a healthy RBC under white light illumination and the image of the unfocused speckle obtained from the same cell under laser tilted illumination. The speckle pattern provided by the laser beam is recorded for 1 second at high frame rate (2000 fps). This high acquisition frame rate allows proper sampling of the cell membrane flickering due to the thermal vibration [24]. The RBCs are introduced and dragged to the observation area using a simple microfluidic chip with a single channel cut by a CO_2 laser in a 2 mm Plexiglas sheet and with a glass cover slip glued on the bottom.

Experimental results involved tracking of speckle patterns captured for healthy and infected malaria RBCs. The movies were recorded moving the microfluidic chip with the cells upside by different distances: 2, 20 and 50 µm respectively. Data processing produced similar results in terms of discrimination between infected and healthy cells.

#162404 - $15.00 USD Received 3 Feb 2012; revised 15 Mar 2012; accepted 23 Mar 2012; published 18 Apr 2012

3. Sample preparation and data analysis

Donor blood was kindly provided by the Blood Bank Service of Azienda Ospedaliero-Universitaria Ospedali Riuniti di Trieste (nonprofit organization for blood donation). Citrate-anticoagulated blood was obtained from healthy A-positive donors after informed consent. Aliquots of blood were centrifuged at 2300 rpm for 13 min to remove the buffy coat and the erythrocyte pellet was washed three times with 5 mM phosphate-buffered saline (PBS). *P. falciparum* (W2 strain) culture was carried out according to Trager and Jensen [34] and maintained at 5% hematocrit (human type A-positive red blood cells) in RPMI 1640 medium with the addition of 1% AlbuMax, 0.01% hypoxantine, 20 mM Hepes, and 2 mM glutammine. Asynchronous cultures with parasitaemia of 4-5% were diluited to 0.01% final hematocrit, aliquoted into a petri dish and incubated at room temperature. Parasitaemia was checked by Giemsa staining of a blood smear, before the optical experiments.

We have analyzed 25 cell samples: 12 corresponding with healthy RBCs (hRBC) and 13 with RBCs infected by *P. falciparum* (iRBC). From the recorded speckle pattern movies, we have performed a digital processing in order to define a list of parameters for classifying the RBC samples. Essentially, the processing involves correlation between the secondary speckle patterns of successive frames and from this correlation operation we have extracted various statistical time varying parameters both regarding to the position of the correlation peak as well as to its value. Working with secondary speckle patterns has the advantage that the way their spatial distribution varies with the axial distance is very much dependent on the distance itself and can be estimated in high precision using simple numerical, correlation based, tools.

We have initially defined a list of 27 parameters of interest from which we have extracted a list of 20 useful correlation related parameters which could also be easily numerically calculated. The extracted parameters are depicted in Table 1. This selection obeys to a significance criterion in the values obtained for each parameter and to the simplicity of their numerical extraction.

Table 1. Set of the 20 Inspected Parameters and their Assigned Serial Number

Serial No.	Parameter	Serial No.	Parameter	Serial No.	Parameter	Serial No.	Parameter
1	amp x shift	8	std shift y	15	std speed x	22	mean correlation
2	amp y shift	9	amp x speed	16	std speed y	23	std corr
5	mean shift x	10	amp y speed	17	amp cumulative shift x	25	amp of corr speed
6	mean shift y	13	mean speed x	18	amp cumulative shift y	26	mean of corr speed
7	std shift x	14	mean speed y	21	amp correlation	27	std corr speed

Serial numbers are attached to the 20 parameters and a short description of the corresponding parameter is given to each number. The physical meaning of these parameters is as follows:

- 1, 2: amplitude of the displacement of the correlation peak in x and y respectively.
- 5, 6: mean of the parameters (1, 2), respectively.
- 7, 8: standard deviation (std) of the parameters (1, 2), respectively.
- 9, 10: amplitude of the displacement speed in x and y respectively.
- 13, 14: mean of the parameters (9, 10), respectively.

#162404 - $15.00 USD Received 3 Feb 2012; revised 15 Mar 2012; accepted 23 Mar 2012; published 18 Apr 2012

- 15, 16: standard deviation of the parameters (9, 10), respectively.
- 17, 18: amplitude of the cumulative displacement speed in x and y respectively.
- 21, 22, 23: amplitude, mean and standard deviation, respectively, of normalized corr-value (the normalization is such that the maximal correlation value was one).
- 25, 26, 27: amplitude, mean and standard deviation, respectively, of speed of corr-value.

Some of the 20 parameters for one of the 12 measured hRBCs can be seen in Figs. 2(a)–2(d) where we show the displacement of the correlation peak in X-Y plane (upper figure) and specify the histograms of X and Y displacements respectively (two lower charts). In Fig. 2(a) we talk about the relative displacement i.e. the change in position between two adjacent temporal frames. In Fig. 2(b) we repeat the same presentation for the speed of movement for the correlation peak. In Fig. 2(c) we repeat the presentation as in Fig. 2(a) but for the accumulative displacement, i.e. in comparison to the first frame of measurement. In Fig. 2(d) in the upper plot we show the correlation value versus the frame number and in the lower plot we show the histogram for the upper chart.

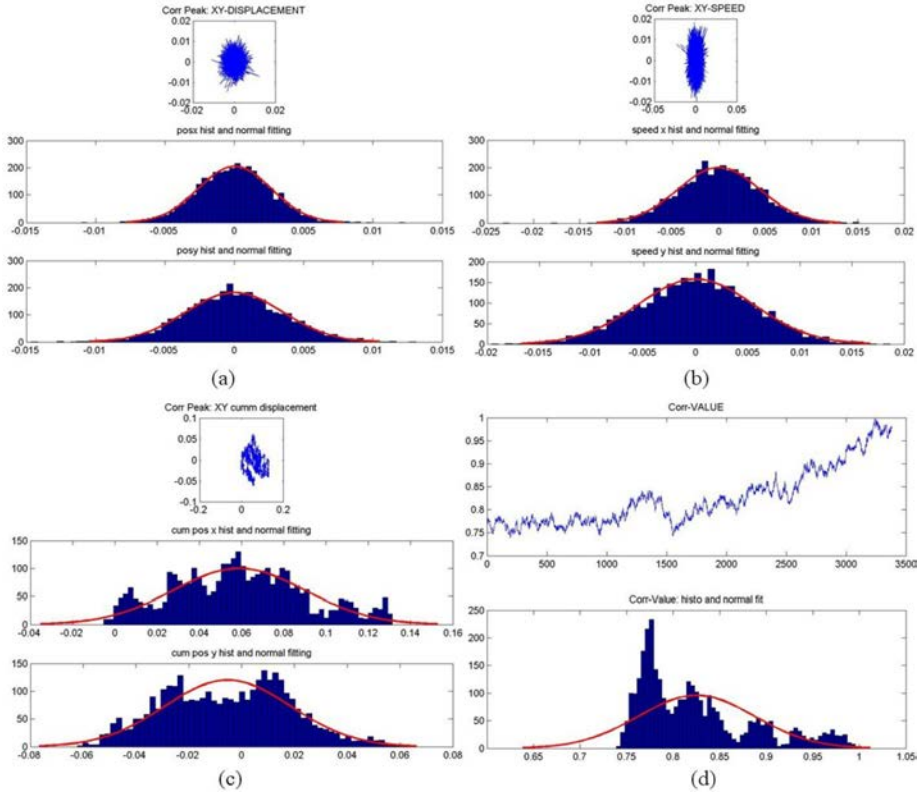

Fig. 2. Some examples of the 20 relevant parameters corresponding to an inspected healthy RBC.

Note that the difference between the computation of a given parameter or an accumulative value for the same parameter (e.g. the amplitude of the shift) is as follows:

$$x_n = pos^{max}\{s_n \otimes s_{n-1}\}, \quad x_n^{cum} = \sum pos^{max}\{s_n \otimes s_{n-1}\}, \tag{1}$$

where x_n is the position of the correlation peak when correlating ($\otimes$) the region of interest in frame n with the one in frame n-1 and x_n^{cum} is the cumulative shift which is the position of the peak when correlating frame n with frame 1. The velocity (regular or cumulative) is computed

#162404 - $15.00 USD Received 3 Feb 2012; revised 15 Mar 2012; accepted 23 Mar 2012; published 18 Apr 2012

by dividing the difference in the amplitude of the shift (regular or cumulative) in units of time. In Fig. 3(a) we present a microscope image of an iRBC obtained under white light illumination and in Fig. 3(b) we show the speckle pattern with the laser illumination.

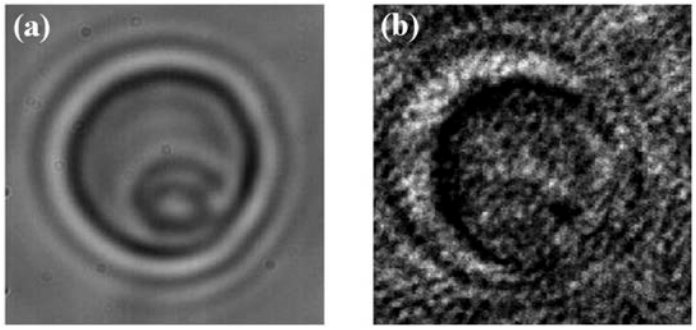

Fig. 3. (a). Microscope image of an infected RBC. (b). Speckle pattern

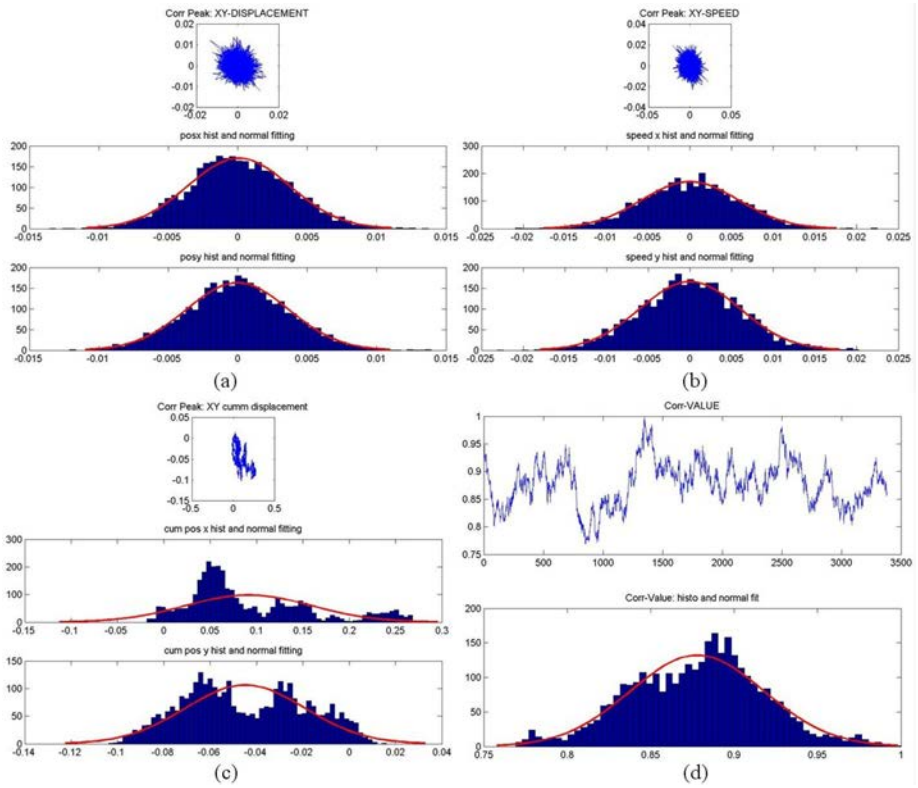

Fig. 4. Some examples of the relevant 20 parameters for one of the infected RBC.

Similarly to Fig. 2, Figs. 4(a)–4(d) present the same parameters shown in Fig. 2 for a hRBC, but now considering the iRBC shown in Fig. 3.

Comparing the parameters shown in Figs. 2 and 4 for hRBC and iRBC respectively, one can notice some differences, e.g. the amplitude of the cumulative displacement XY for the infected RBC is larger than for the healthy RBC, the range and the distribution of the correlation values are also different. Nevertheless, those changes are small and not always consistent in all the measurements and thus a more sophisticated numerical analysis tools had to be developed. In the next two sections we present two of such numerical tools and we discuss their capabilities to discriminate hRBC from the iRBC.

#162404 - $15.00 USD Received 3 Feb 2012; revised 15 Mar 2012; accepted 23 Mar 2012; published 18 Apr 2012

4. Malaria diagnostics via fuzzy logic

After proper inspection of the collected data when considering a defocusing distance of 2 μm away from the RBCs focus plane, we have constructed the fuzzy logic algorithm for processing the recordings made. Straight forward comparison of data between infected and healthy samples leads to no conclusive decision criteria whereas a set of values is associated with an infected or a healthy RBC, as discussed above for two samples and demonstrated for all the samples when considering 4 of the 20 parameters shown in Figs. 5 and 6.

Note that defocus affects the accuracy of measurement since it affects the size of the generated speckle patterns. Moreover, the accuracy in estimating the Z (axial) axis movement strongly depends on the defocusing distance since if the distance is too large Z movement will not affect the distribution of the speckle patterns at all. In our case, we captured images in several close distances and tried to analyze all of them and eventually optimized our system by choosing the distance providing the best detection performance.

Looking at the data, there's no clear Boolean rule to differentiate between healthy and infected cells, more so, any rule that is based on a comparison between two particular samples (one healthy and one infected) will not be valid for all other pairs of samples. This leads us to seek a flexible inference engine based on a combination of samples, and so we turn to fuzzy logic. Fuzzy logic, first introduced by Zadeh [35] addresses, among other things, problems where Boolean logic fails to give a solution due to its roughness and a more flexible logic is required. In fuzzy logic inferencing we first have to establish a set of rules [36], based on the data.

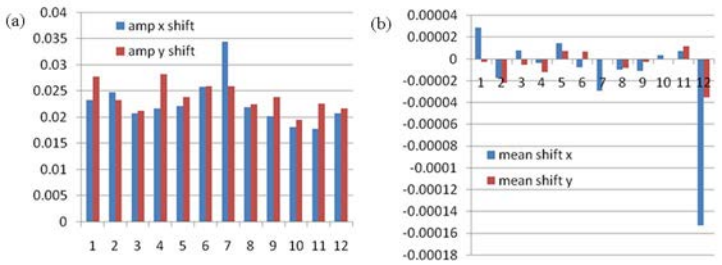

Fig. 5. An example of 4 parameters measured for the 12 hRBC (healthy cell samples).

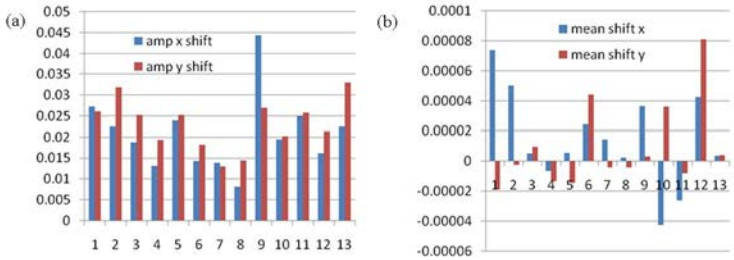

Fig. 6. An example of 4 parameters measured for the 13 iRBC (infected cells samples)

For this reason we need to pick part of the data as the basis of our rules. We have decided to calculate the average values considering the top first 5 samples for each of the 20 parameters, for data from healthy and infected RBCs.

The reason why 5 samples are taken is because 5 is sufficiently large that the average value has an actual meaning but sufficiently small to leave enough data to be manipulated by the fuzzy logic rules generated by these 5 samples. We then reorder the 20 parameters in Table 1 according to the averaged parameter values, from the biggest (left) to the smallest (right) as shown in Table 2 (hRBC) and Table 3 (iRBC), respectively.

#162404 - $15.00 USD Received 3 Feb 2012; revised 15 Mar 2012; accepted 23 Mar 2012; published 18 Apr 2012

Table 2. Parameter ordering for hRBCs from the highest to the smallest

Serial No.	Averaged value	Serial No.	Averaged value	Serial No.	Averaged value	Serial No.	Averaged value
21	19.188795	10	0.0390519	16	0.0056608	26	1.45E-05
22	0.897064	9	0.0378490	15	0.0050566	5	6.03E-06
18	0.161484	25	0.0337874	27	0.0043080	13	2.70E-08
17	0.107936	2	0.0248739	8	0.0034421	14	–8.15E-07
23	0.040245	1	0.0225327	7	0.0030422	6	–6.98E-06

Table 3. Parameter ordering for iRBCs from the highest (left) to the smallest (right)

Serial No.	Averaged value	Serial No.	Averaged value	Serial No.	Averaged value	Serial No.	Averaged value
21	19.998107	23	0.038407	16	0.005445	5	2.56E-05
22	0.900882	25	0.038133	15	0.004723	13	1.40E-07
17	0.136950	9	0.034826	27	0.004609	14	–6.08E-07
18	0.102413	2	0.025549	8	0.003423	26	–4.66E-06
10	0.039440	1	0.021121	7	0.002880	6	–7.95E-06

As can be seen, while several parameters remain in the same relative position for either healthy or infected cells (the black serial numbers), others swap places, e.g., parameter 14 has bigger value than parameter 26 for healthy RBCs but smaller values for infected RBCs.

We have decided to focus on three pairs of parameters that seemed to have the greatest potential for differentiating between the healthy and infected cells: (18,17), (9,25) and (26,14), shown in boldface, in Table 4.

Table 4. Unified parameters ordering for hRBC (first row) and iRBC (second row) and selection of three pairs of parameters for processing (bold)

21	22	**18**	**17**	23	10	**9**	**25**	2	1	16	15	27	8	7	**26**	5	13	**14**	6
21	22	**17**	**18**	10	23	**25**	**9**	2	1	16	15	27	8	7	5	13	**14**	**26**	6

According to the ordering rule shown in Table 4, hRBC cell should have larger values for parameter 26 than for parameter 14, larger values for parameter 9 than for parameter 25 and larger values for parameter 18 than for parameter 17. However, if we take a look at the partial data depicted in Fig. 7 and Fig. 8, representing the three pairs of selected parameter for the first 5 samples used to calculate the averaged values, we observe that the reordering rule does not fit to all the samples. For example, Sample2 from hRBC and Sample3 from iRBC have two pairs that do not respect the ordering rules derived by averaging the values. Note that except for Sample5 of healthy cells, none of the samples individually obey all the rules. This is the advantage of fuzzy logic, the total conclusion (as given later on) may be correct even if some of the rules are not met.

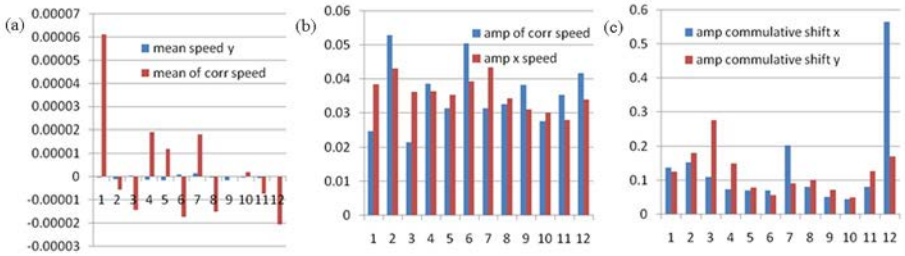

Fig. 7. Three pairs of parameters for the healthy cell samples. The first 5 samples are used to determine the rules. Notice that some cells do not fit the reordering rule derived by averaging.

#162404 - $15.00 USD Received 3 Feb 2012; revised 15 Mar 2012; accepted 23 Mar 2012; published 18 Apr 2012

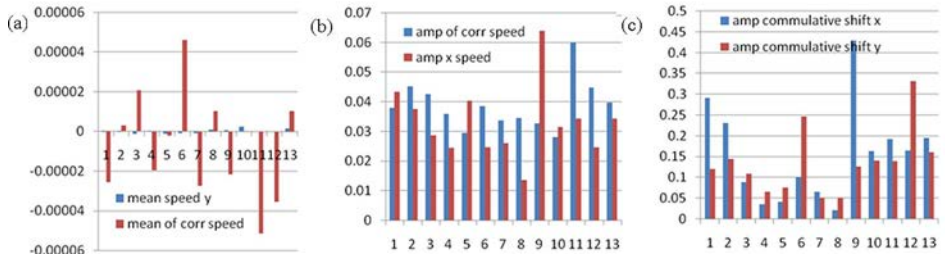

Fig. 8. Three pairs of parameters for the infected cell samples. The first 5 samples are used to determine the rules. Notice that some cells do not fit the reordering rule derived by averaging.

Since Boolean rules are not sufficient to make the decision whether a cell is infected or not, according to the three parameter-pairs chosen, we establish fuzzy logic rules that combine the 3 pairs of columns in a $5 \times 5 \times 5$ 3D rule matrix, like the one given in Fig. 5 [37]. Note that the rule matrix contains fuzzy terms such as very small, medium etc. A typical fuzzy rule may be "if ratio of columns 26 and 14 is small and the ratio of columns 9 and 25 is very large and the ratio of columns 18 and 17 is very small then the outcome is 3 (corresponding to large)". This rule can be seen in Fig. 9, when addressing the second column and the fifth row of the first (leftmost) 2D matrix.

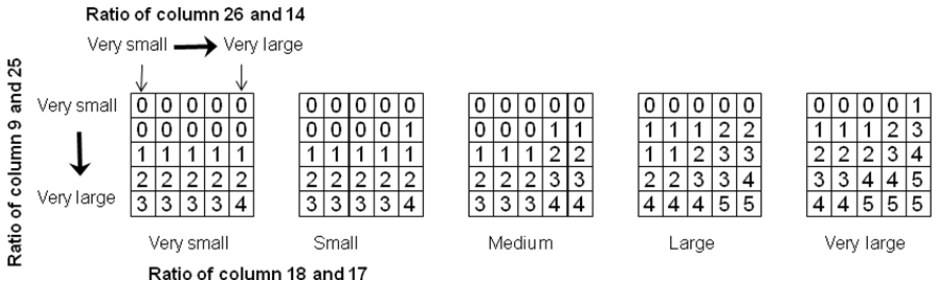

Fig. 9. Fuzzy logic ruling.

We assume that a 3-valued vector represents the input for each cell and generates a 3D Gaussian being shifted according to the vector's elements. A 2D example of such a shift and how it is represented is given in Fig. 10.

Then, the 6 parameters (3 pairs) for each sample are fed into the fuzzy logic inference engine. The result is a number indicating the grade given to the current sample. We then take the average of the 3 parameter-pairs for the test group and obtain a reference grade. If the grade of a specific sample is larger than the reference grade then we diagnose the person as a member of the group. This is done separately on the list of cells that are healthy and those which are infected. The outcome is given in Fig. 11, where cells correctly diagnosed for being healthy are drawn in green and cells correctly diagnose for being infected are drawn in red.

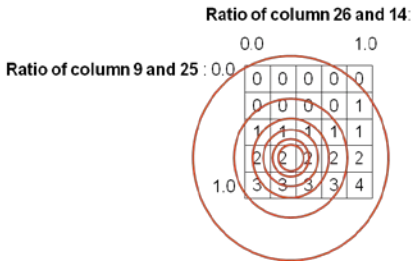

Fig. 10. An example of applied Gaussian weighting.

#162404 - $15.00 USD Received 3 Feb 2012; revised 15 Mar 2012; accepted 23 Mar 2012; published 18 Apr 2012

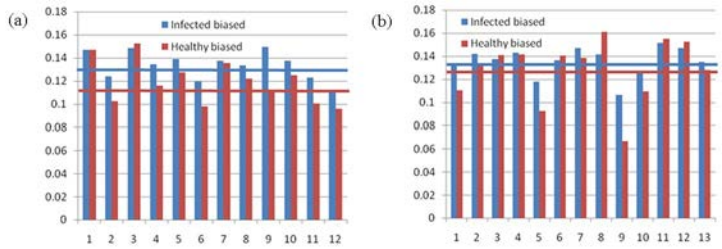

Fig. 11. Results for the fuzzy logic processing: (a) 8 of 12 samples are correctly diagnosed for being healthy (above at list one threshold line) and (b) 9 of 13 samples are correctly diagnosed for being infected (below at least one threshold line).

The result is that we correctly identify 67% of the healthy cells and 69% of the infected cells. Note that healthy Sample2 that was previously marked for not obeying two rules is indeed not identified as healthy, but infected Sample3 which was previously marked for not obeying two rules is identified as infected, as required.

Note that if one wishes to use fuzzy logic approach for detecting other types of cells, one may have to change the rules because other types of cells may be better characterized by different physical parameters and even if the same physical parameters are good as well, it might be that different range of values better express their physical properties. In order to properly adapt the rules to the type of problem being investigated, it is always recommended (as we also did in this paper) to take a few measurements as references used for the rules definition. Then, after properly extracting the rules, to apply the formulated mechanism over the rest of the measurements in order to validate the functionality of the approach for the new types of cells.

5. Principal components analysis

Principal component analysis (PCA) is a mathematical procedure that uses an orthogonal transformation to convert a set of observations of possibly correlated variables into a set of values of uncorrelated variables called principal components [38,39]. The number of principal components is less than or equal to the number of original variables. This transformation is defined in such a way that the first principal component has variance as high as possible (that is, accounts for as much of the variability in the data as possible), and each succeeding component in turn has the highest variance possible under the constraint that it will be orthogonal to (uncorrelated with) the preceding components.

Principal components are guaranteed to be independent only if the data set is jointly normally distributed. PCA is sensitive to the relative scaling of the original variables. Often, its operation can be thought of as revealing the internal structure of the data in a way which best explains the variance in the data. If a multivariate data set is visualized as a set of coordinates in a high-dimensional data space (1 axis per variable), PCA can supply the user with a lower-dimensional picture, a “shadow” of this object when viewed from its (in some sense) most informative viewpoint. This is done by using only the first few principal components so that the dimensionality of the transformed data is reduced.

5.1. First analysis

The first step was searching different behaviors of the data for each one of the three distances at which speckle data were recorded, i.e., at distances of 2 μm, 20 μm and 50 μm. So the data was arranged on three graphs, where each one of the 20 parameters (which measure different data in different units) was represented by an index on the x-axis, and the value of the examination is given on the y-axis. Red triangles represent the infected cells while the green marking the healthy one. For data taken from 50 μm distance, many of the parameters have the result as seen in Fig. 12 where one see that the healthy cells values distribute rather normal, while the infected ones have more spread values.

#162404 - $15.00 USD Received 3 Feb 2012; revised 15 Mar 2012; accepted 23 Mar 2012; published 18 Apr 2012

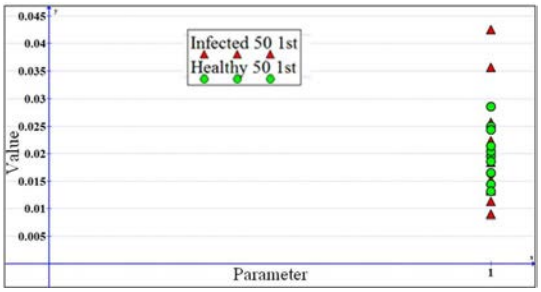

Fig. 12. Values of parameter 1 of healthy and infected cells for data taken at a distance of 50 μm.

It seems that many values of healthy cells have smaller variance than the infected ones. Therefore, PCA can be a very good method to recognize some discrimination between the two types of cells. The best discrimination has been found to occur for data collected from distance of 50 μm.

5.2. Data standardization

The first step when operating the PCA on the data is normalizing it. As observed in Figs. 13(a) and 13(b), not all variables have the same scale. The PCA calculates the covariance of every two variables, so operating it with non-normalized data will give an unwanted advantage to variables with larger scales. The x-axis is the number of variable (as previously noted we have 20) and the y-axis is the value it receives. One can easily see that the variable noted as "15" has much larger scale than others, and other variables have also many scales of themselves.

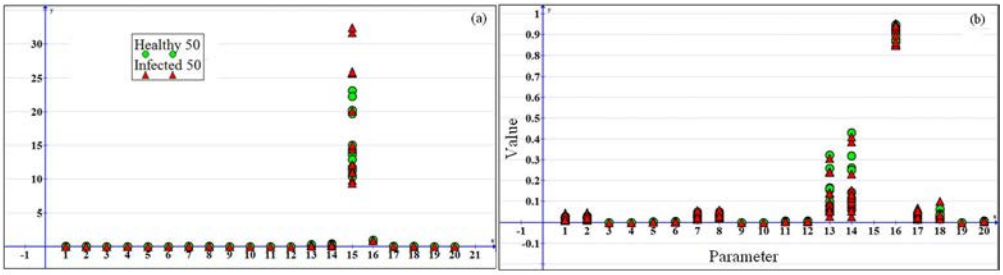

Fig. 13. (a). Parameter 15 compared to others for distance of 50 μm. (b). All parameters and values for distance of 50 μm.

Normalization converts the data to be with zero average and standard deviation of 1, i.e. for a normalized data it is needed to subtract the mean (average) and then divide it with the standard deviation to rescale the data. This procedure has to be done for each column (every variable). Let us denote by Z the new standardized matrix. In Fig. 14 one may see the normalized data.

5.3s Eigenvalues and eigenvectors

The covariance matrix C has eigenvalues and eigenvectors, which one can calculate. Let D be the diagonal matrix of the eigenvalues of C, and let V be the matrix of the eigenvectors (as columns). To understand the meaning of these eigenvalues, it is essential to rearrange them decreasingly and also the eigenvectors as columns in a matrix, respectively.

Now, each eigenvalue represents one dimension. The first (and now, the greatest) eigenvalue represents the first principal component—the dimension that explains more of the variance than others. The second one represents the second principal component, and so on.

#162404 - $15.00 USD Received 3 Feb 2012; revised 15 Mar 2012; accepted 23 Mar 2012; published 18 Apr 2012

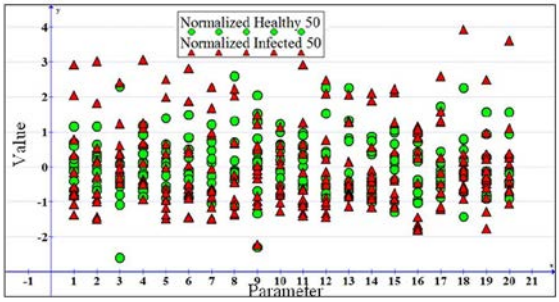

Fig. 14. Normalized data.

To explain enough of the variance, it is needed to calculate the cumulative sum of the eigenvalues. If *D* is the matrix above (with decreasing values), then for every *i*,

$$\frac{\sum_{i=1}^{n} D_{ii}}{tr(D)} \tag{2}$$

calculates the cumulative sum. For instance, in the 50 μm distance results, the first 15 eigenvalues of *C* are {9.40, 2.64, 2.43, 1.32, 1.12, 0.94, 0.75, 0.60, 0.38, 0.11, 0.09, 0.06, 0.05, 0.02, 0.01}. It is easily seen that the sum of the first 5 values covers most of the cumulative sum. Indeed, their cumulative sum is 0.85. 85% seems to be accurate enough, so now it is needed to make a new matrix, based on the first 5 eigenvectors matching the first 5 eigenvalues: $M = [v_1, v_2, \ldots, v_5]$.

5.4 Forming the new data

After having the matrix *M* above, all needed is multiplying the original normalized data matrix *Z*, with *M* from the right: $S = Z \times M$. The next step is calculating the length of each vector (which is a point in the new 5-dimensional space). The formula

$$\rho_i = \sqrt{(SS')_{ii}} \tag{3}$$

gives the length of the i-th vector in the new space. The last step is finding the radius that separates the two populations. Plotting the length of the vectors versus index yields the graph of Fig. 15. In this figure the horizontal axis is the patient (12 healthy and 12 infected) and the vertical one is the computed ρ_i.

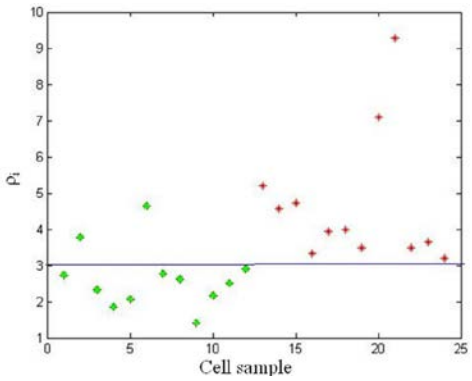

Fig. 15. Separation between infected and healthy cells. The figure presents the plot of the length of the vectors versus the index.

#162404 - $15.00 USD Received 3 Feb 2012; revised 15 Mar 2012; accepted 23 Mar 2012; published 18 Apr 2012

The green points represent healthy cells, and the red are the infected. Thus, from the last result one may see that there is 100% probability that the cell is infected when $\rho i>3$. There is 83% probability (10 out of 12 patients) that the cell is healthy if $\rho i<3$.

Note that basically there is no relation between the fuzzy logic and the PCA techniques that were presented in this paper (the fuzzy logic is not a prerequisite before applying PCA) and they are more or less orthogonal in their decision making process. However, this is exactly why we used both. We think that because the two approaches are very different the combination of both of them may result in overall better detection performance. Although in general the fuzzy logic did not as good as PCA but it did well in different types of cells and thus smart combination of both techniques in the overall decision making process may produce a more noise immune algorithm capable of detecting infected cells in their earlier stages and with higher detection probability and lower probability for false alarm.

Also note that biomechanical properties of iRBCs are severely altered during the disease progress (from ring, to trophozoite, and to schizont stages), and thus flickering of iRBCs are different during this alteration. For example, the flickering of iRBCs in early stage (ring) is similar to hRBCs and the flickering of iRBCs at very late stage (schizont) is very little. In this study we tried to inspect RBC in different stages of the disease and indeed we also saw preliminary and encouraging results indicating that with the proposed approach we will be able not only to detect if the cell is infected but also to detect the stage of the disease. However, those results were less controlled (since we ourselves were also not 100% sure about the exact stage of the disease) and this we decided to avoid using those results in the preliminary proof of concept stage being presented in this paper. Our current task without a doubt is to extend the proposed principle and algorithms also for detecting the exact stage of the disease and this will be the aim of our next paper.

6. Conclusions

In this paper we were present a new optical technique based upon processing of speckles statistics in order to detect malaria. The processing was based upon construction of fuzzy logic based ruling and principle component analysis applied on correlation related manipulation of the time varying speckle patterns. Preliminary experimental results showed high capability of detection of infected cells (100% probability using PCA analysis). The combination between the fuzzy logic and the PCA analysis can provide also good results in detection of healthy cells (both techniques produce errors for different samples).

Acknowledgments

The authors thank Dr. Elena Bevilacqua and Dr. Luca Mascaretti (Blood Bank Service of Azienda Ospedaliero-Universitaria Ospedali Riuniti di Trieste) for providing fresh blood and Prof. Donatella Taramelli (University of Milan) for providing the *P. falciparum* sample. S. F. acknowledges the grant from Area Science Park of Trieste.